Numerical simulations of hydraulic jumps with the Shear Shallow Water model

Argiris I Delis, Hervé Guillard, Yih-Chin Tai

SMAI-JCM
SMAI Journal of Computational Mathematics

Numerical simulations of hydraulic jumps with the Shear Shallow Water model

Argiris I. Delis, Hervé Guillard & Yih-Chin Tai

Volume 4 (2018), p. 319-344.
<http://smai-jcm.cedram.org/item?id=SMAI-JCM_2018__4__319_0>

SMAI Journal of Computational Mathematics
Vol. 4, 319-344 (2018)

Numerical simulations of hydraulic jumps with the Shear Shallow Water model

Argiris I. Delis [1]
Hervé Guillard [2]
Yih-Chin Tai [3]

[1] School of Production Engineering and Management, Technical University of Crete, University Campus, Chania, Crete, Greece
E-mail address: adelis@science.tuc.gr
[2] Inria Sophia Antipolis Méditerranée and Côte d'Azur University, LJAD, CNRS, France
E-mail address: herve.guillard@inria.fr
[3] Departement of Hydraulic and Ocean Engineering, National Cheng Kung University, Tainan 701, Taiwan
E-mail address: yctai@mail.ncku.edu.tw.

Abstract. An extension and numerical approximation of the shear shallow water equations model, recently proposed in [25], is considered in this work. The model equations are able to describe the oscillatory nature of turbulent hydraulic jumps and as such correct the deficiency of the classical non-linear shallow water equations in describing such phenomena. The model equations, originally developed for horizontal flow or flows occurring over small constant slopes, are straightforwardly extended here for modeling flows over non-constant slopes and numerically solved by a second-order well-balanced finite volume scheme. Further, a new set of exact solutions to the extended model equations is derived and several numerical tests are performed to validate the numerical scheme and its ability to predict the oscillatory nature of hydraulic jumps under different flow conditions.

Keywords. Shear Shallow Water model, Shallow Water equations, Turbulent Hydraulic jumps, Free surface flows, Finite Volumes, Well-balancing.

1. Introduction

Hydraulic jumps are commonly observed in laboratory experiments, river flows or coastal areas. The classical description of this phenomenon uses the shallow water hyperbolic system of equations (SWE) and assimilates hydraulic jumps to a discontinuity of zero length governed by jump relations between the supercritical upstream state and the subcritical downstream one as:

$$\begin{aligned} &[h(u-D)] = 0; \\ &[hu(u-D) + gh^2/2] = 0 \end{aligned} \tag{1.1}$$

where here $[\cdot]$ stands for the jump $(\cdot)_R - (\cdot)_L$ between the upstream state $(\cdot)_L$ and the downstream one $(\cdot)_R$, h is the water height, u the flow velocity, g the gravity acceleration and D the jump velocity. This classical description of hydraulic jumps has well-known shortcomings. As observed in many laboratory experiments, see e.g [4], hydraulic jumps have a non-zero width and their shapes are different according to the upstream Froude number. In particular, for large Froude numbers (typically larger than 1.7) the jump becomes turbulent; the water depth rapidly increases, large scale turbulent eddies, forming a roller, appear beneath the free surface and intense vorticity generation is observed. Oscillations with well-defined frequencies of the toe of the hydraulic jump have been also reported [22, 5].

Building on an earlier work devoted to roll waves in [24], and more recently in [16], Richard and Gavrilyuk have proposed in [25] a new model for turbulent hydraulic jumps, called the Shear Shallow

Water Equations (SSWE), that attempt to correct most of the deficiencies of the classical shallow water description of these phenomena. In particular, their model is able to compute the jump's toe oscillations with a frequency that compare reasonably well with experiments. This SSWE model was obtained by taking into account the fluctuation of the horizontal velocity along the vertical direction. This model is also interesting since it contains only two adjustable parameters with a well-defined physical interpretations. These two parameters, namely the wall enstrophy ϕ and the energy dissipation coefficient C_r have been determined in Richard and Gavrilyuk's model from the experiments by Hager and Bremen [13].

The model of [25] has been developed for horizontal flows or flows occurring on a small constant slope. The main purpose of this work is to investigate, also numerically, a straightforward extension of this model for flows on non-constant slopes. In particular, no attempts have been made to adjust the parameters of the model to this new situation hence, we compute these values as proposed in [25]. The remainder of this paper is the following: In Section 2, we recall some salient features of the model proposed in [25] and describe its extension for flows over a non-constant topography. Then, in Section 3, we describe the numerical method used to approximate the solutions of the model. Actually, the model of [25] is a conservative hyperbolic system with a stiff source term whose approximation is not straightforward. The design of a second-order (in space and time) finite volume numerical scheme used for its extension on non-constant topography necessitates to integrate some modifications related to the preservation of equilibrium (lake at rest) solutions. In the last section, we present some numerical tests and corresponding results. Some new analytic solutions of the SSWE over non-constant topography are derived, by modifying some well-known benchmark cases used in shallow water and open channel flow studies. This consists another novel aspect of this work. Finally, a numerical comparison with experimental data from a forced hydraulic jump is also presented.

2. The shear shallow water model

For a detailed derivation of this model, we refer to [24] and [25] and here briefly summarize the rationale leading to this model. The shallow water model uses the conservation of mass and momentum and thus does not consider explicitly the physical principle of energy conservation. In contrast, the SSWE deals explicitly with the conservation of energy that is split into three components: kinetic, potential and turbulent energy, the latter being associated with the fluctuation of the horizontal velocity along the vertical direction. For hydraulic jumps, these fluctuations are themselves associated with the presence of small scale vortices near the bottom associated to the boundary layer and to the existence of a large scale roller close to the water surface. Using physical arguments, the turbulent energy is expressed in term of a variable called enstrophy with two components : a small scale enstrophy ϕ_s associated with the near bottom boundary layer and a large scale enstrophy Ψ associated with the roller flow. Incorporating in this description, a space varying bottom topography, $b \equiv b(x)$ leads to the following system written in one-dimensional conservative form [25] :

$$\partial_t \mathbf{U} + \partial_x \mathbf{F}(\mathbf{U}) = \mathbf{S}_b + \mathbf{S}_f, \tag{2.1}$$

where the vectors of conserved variables $\mathbf{U}$, fluxes $\mathbf{F}$ and source terms $\mathbf{S}_b$ and $\mathbf{S}_f$ are defined as

$$\mathbf{U} = \begin{pmatrix} h \\ q \\ E \end{pmatrix}, \ \mathbf{F} = \begin{pmatrix} q \\ \dfrac{q^2}{h} + P \\ q(E+P)/h \end{pmatrix}, \ \mathbf{S}_b = \begin{pmatrix} 0 \\ -gh\partial_x b \\ 0 \end{pmatrix}, \ \mathbf{S}_f = \begin{pmatrix} 0 \\ -C_f \dfrac{|q|q}{h^2} \\ -\left(C_f + C_r \dfrac{\Phi - \phi_s}{\Phi}\right) \dfrac{|q|^3}{h^3} \end{pmatrix} \tag{2.2}$$

with h being the water depth, $q = hu$ the unit discharge, u the average velocity, Φ the total enstrophy and is E the total energy defined as

$$E = h\frac{u^2}{2} + g\frac{h^2}{2} + ghb + \Phi\frac{h^3}{2}.$$

In this relation, the first two terms represent, respectively, the kinetic and potential energies while the last one stands for a turbulent energy defined thanks to the total enstrophy Φ. For more details on the physical interpretation of the model we refer to [25]. Further, P is the pressure given as

$$P = \frac{gh^2}{2} + \Phi h^3.$$

By defining an "internal energy", e, by

$$e = \frac{gh}{2} + gb + \Phi\frac{h^2}{2},$$

the following equation of state can be verified

$$P = 2he - \frac{gh^2}{2} - 2ghb = 2E - hu^2 - \frac{gh^2}{2} - 2ghb.$$

The two source terms in (2.1) $\mathbf{S}_b$ and $\mathbf{S}_f$ stand, respectively, for the topography and the friction terms. In the latter, C_f is the friction coefficient, related to the Darcy-Weisbach coefficient f by $C_f = f/8$ and C_r is a drag coefficient corresponding to the dissipation of the entrophy in the turbulent roller generated in a hydraulic jump. Further, the total enstrophy is decomposed as

$$\Phi = \Psi + \phi_s$$

where ϕ_s is the small scale enstrophy describing the intensity of the vortices in the boundary layer near the bed, and Ψ is the large scale (roller) enstrophy. Moreover, it can be seen that system (2.1) implies the following equation for the enstrophy

$$\partial_t\Phi + u\partial_x\Phi = -\frac{2}{h^3}C_r\frac{\Phi - \phi_s}{\Phi}|u|^3. \tag{2.3}$$

System (2.1) admits the following quasi-linear form, setting $\mathbf{W} = (h, u, \Phi)^{\mathrm{T}}$,

$$\partial_t\mathbf{W} + \mathbf{A}\partial_x\mathbf{W} = \widetilde{\mathbf{S}}_b + \widetilde{\mathbf{S}}_f$$

where

$$\mathbf{A} = \begin{pmatrix} u & h & 0 \\ g + 3h\Phi & u & h^2 \\ 0 & 0 & u \end{pmatrix}, \quad \widetilde{\mathbf{S}}_b = \begin{pmatrix} 0 \\ -g\partial_x b \\ 0 \end{pmatrix}, \quad \widetilde{\mathbf{S}}_f = \begin{pmatrix} 0 \\ -C_f\dfrac{|u|u}{h} \\ -\dfrac{2}{h^3}C_r\dfrac{\Phi - \phi_s}{\Phi}|u|^3 \end{pmatrix}.$$

The characteristic polynomial of $\mathbf{A}$ is then given as

$$\chi(\mathbf{A}) = (u - \lambda)\left((u - \lambda)^2 - (gh + 3\Phi h^2)\right)$$

with roots $\lambda_1 = u - \alpha, \quad \lambda_2 = u, \quad \lambda_3 = u + \alpha$ where $\alpha = \sqrt{gh + 3\Phi h^2}$, verifying the hyperbolic nature of system (2.1).

An important property of (2.1), related to the source terms, is that admits non-trivial steady-states. Following from (2.1), these may be given as

$$\partial_x q = 0$$
$$q\partial_x u + gh\partial_x(h+b) + \partial_x(\Phi h^3) = -C_f \frac{|q|q}{h^2}$$
$$\partial_x(u(E+P)) = -\frac{2}{h^3} C_r \frac{\Phi - \phi_s}{\Phi} \frac{|q|^3}{h^3}$$

From the above equilibria, some classes of steady-state solutions can be derived which can help to asses the performance of a numerical scheme and will be considered later on in Section 4.3.

An important elementary solution is the so-called flow at rest that is easily obtained assuming $u = q = 0$ and $h + b = \eta(x, 0) = \eta_0$ (constant). For the SSWE we see that from the momentum equation a steady equilibrium is obtained in this case if the enstrophy verifies also

$$\partial_x(\Phi h^3) = 0.$$

This relation is verified if $\Phi = 0$ that is consistent with the physical requirement that no large or small scale enstrophy is created in the stagnant water case. Therefore,$\mathbf{W}_0 = (\eta_0 - b,\ 0,\ 0)^{\mathrm{T}}$ defines a class of exact steady solution of the model.

3. Numerical method

We describe here a relatively simple finite volume (FV) scheme for system (2.1) that is of second-order accuracy in space and time and is well-balanced in the sense of preserving exactly the flow at rest solution thus allowing to have an efficient treatment of the topography source term [1, 28]. In practice, schemes preserving this equilibrium (also called the $\mathcal{C}$-propery) give good results even in unsteady cases [8]. In this FV scheme a splitting method is adopted where at the first step we solve the system of equations without the drag term $\mathbf{S}_f$ and the well-balanced spatial discretization is utilized. At the second step in the splitting method, we take into account the friction term and a system of ordinary equations is to be solved. For this, we will use the fact that due to the special structure of system (2.1) these ODEs can be solved in an exact way.

3.1. Advection step and well-balancing

At the first step of the splitting, we consider the following semi-discrete form of the FV scheme for the convection terms and topography source term $\mathbf{S}_b$

$$\Delta x \partial_t \mathbf{U}_i + \mathbf{F}_{i+1/2} - \mathbf{F}_{i-1/2} = \mathbf{S}_b^{i+1/2} + \mathbf{S}_b^{i-1/2} \tag{3.1}$$

where $i = 1, \ldots, N$ refers to the center of the computational cell $I_i = [x_{i-1/2}, x_{i+1/2}] = [x_i - \frac{1}{2}\Delta x, x_i + \frac{1}{2}\Delta x]$, $\mathbf{F}_{i\pm1/2}$ are the numerical fluxes at the cell's interfaces $i \pm 1/2$. To design the topography source terms discretisations at the cell interfaces, $\mathbf{S}_b^{i\pm1/2}$, we need to specify first the form of the numerical fluxes. In this work, we consider the classical Rusanov numerical flux which writes as

$$\mathbf{F}_{i+1/2} = \frac{1}{2}\left(\mathbf{F}(\mathbf{U}_{i+1/2}^R) + \mathbf{F}(\mathbf{U}_{i+1/2}^L)\right) - \frac{\mathcal{C}_{i+1/2}}{2}\left(\mathbf{U}_{i+1/2}^R - \mathbf{U}_{i+1/2}^L\right) \tag{3.2}$$

where $(\cdot)_{i+1/2}^L$ and $(\cdot)_{i+1/2}^R$ denote the left and right (possibly reconstructed) solution and topography values at the $i + 1/2$ interface and

$$\mathcal{C}_{i+1/2} = \sup_{\mathbf{U}=\mathbf{U}_{i+1/2}^{R,L}} \left(\sup_{j=1,2,3} |\lambda_j(\mathbf{U})| \right)$$

with λ_j being the eigenvalues of the system. For a first-order spatial scheme one has $\mathbf{U}^R_{i+1/2} = \mathbf{U}_{i+1}$ and $\mathbf{U}^L_{i+1/2} = \mathbf{U}_i$.

Now, plugging the numerical flux expression (3.2) in the scheme (3.1) and after some simple manipulations, we can write it in the following fluctuation form

$$\begin{aligned}\Delta x \partial_t \mathbf{U}_i &+ \frac{1}{2}\left(\mathbf{F}(\mathbf{U}^R_{i+1/2}) - \mathbf{F}(\mathbf{U}^L_{i+1/2})\right) + \mathbf{F}(\mathbf{U}^L_{i+1/2}) - \mathbf{F}(\mathbf{U}_i) - \frac{\mathcal{C}_{i+1/2}}{2}\left(\mathbf{U}^R_{i+1/2} - \mathbf{U}^L_{i+1/2}\right)\\ &+ \frac{1}{2}\left(\mathbf{F}(\mathbf{U}^R_{i-1/2}) - \mathbf{F}(\mathbf{U}^L_{i-1/2})\right) - \mathbf{F}(\mathbf{U}^R_{i-1/2}) + \mathbf{F}(\mathbf{U}_i) + \frac{\mathcal{C}_{i-1/2}}{2}\left(\mathbf{U}^R_{i-1/2} - \mathbf{U}^L_{i-1/2}\right)\\ &= \mathbf{S}_b^{i+1/2} + \mathbf{S}_b^{i-1/2}.\end{aligned}$$

For the flow at rest equilibrium the above scheme takes the following form, by setting $\partial_t \mathbf{U}_i = 0$ and $u = q = 0$,

$$\begin{aligned}&\frac{1}{2}\begin{pmatrix}0\\ g\bar{h}_{i+1/2}\Delta h_{i+1/2}\\ 0\end{pmatrix} - \begin{pmatrix}0\\ g\bar{h}^-_{i+1/2}\Delta h^-_{i+1/2}\\ 0\end{pmatrix} - \frac{\mathcal{C}_{i+1/2}}{2}\begin{pmatrix}\Delta h_{i+1/2}\\ 0\\ g\bar{b}_{i+1/2}\Delta h_{i+1/2}\end{pmatrix}\\ +\ &\frac{1}{2}\begin{pmatrix}0\\ g\bar{h}_{i-1/2}\Delta h_{i-1/2}\\ 0\end{pmatrix} + \begin{pmatrix}0\\ g\bar{h}^+_{i-1/2}\Delta h^+_{i-1/2}\\ 0\end{pmatrix} + \frac{\mathcal{C}_{i-1/2}}{2}\begin{pmatrix}\Delta h_{i-1/2}\\ 0\\ g\bar{b}_{i-1/2}\Delta h_{i-1/2}\end{pmatrix}\\ =\ &\mathbf{S}_b^{i+1/2} + \mathbf{S}_b^{i-1/2}\end{aligned}$$

where the following simple notations have been used

$$\bar{(\cdot)}_{i\pm1/2} = \frac{(\cdot)^R_{i\pm1/2} + (\cdot)^L_{i\pm1/2}}{2},\quad \bar{(\cdot)}^-_{i+1/2} = \frac{(\cdot)_i + (\cdot)^L_{i+1/2}}{2},\quad \bar{(\cdot)}^+_{i+1/2} = \frac{(\cdot)_{i+1} + (\cdot)^R_{i+1/2}}{2}$$

and

$$\Delta(\cdot)_{i\pm1/2} = (\cdot)^R_{i\pm1/2} - (\cdot)^L_{i\pm1/2},\quad \Delta(\cdot)^-_{i+1/2} = (\cdot)_i - (\cdot)^L_{i+1/2},\quad \Delta(\cdot)^+_{i+1/2} = (\cdot)_{i+1} - (\cdot)^R_{i+1/2}.$$

We note that for a first-order scheme and following from the above notation the terms $g\bar{h}^-_{i+1/2}\Delta h^-_{i+1/2}$ and $g\bar{h}^+_{i-1/2}\Delta h^+_{i-1/2}$ vanish.

Now, the simplest definition of the discrete source terms, guaranteeing that well-balancedness, is achieved are the following

$$\begin{aligned}\mathbf{S}_b^{i+1/2} &+ \mathbf{S}_b^{i-1/2} =\\ &- \frac{1}{2}\begin{pmatrix}0\\ g\bar{h}_{i+1/2}\Delta b_{i+1/2}\\ 0\end{pmatrix} + \begin{pmatrix}0\\ g\bar{h}^-_{i+1/2}\Delta b^-_{i+1/2}\\ 0\end{pmatrix} + \frac{\mathcal{C}_{i+1/2}}{2}\begin{pmatrix}\Delta b_{i+1/2}\\ 0\\ g\bar{b}_{i+1/2}\Delta b_{i+1/2}\end{pmatrix}\\ &- \frac{1}{2}\begin{pmatrix}0\\ g\bar{h}_{i-1/2}\Delta b_{i-1/2}\\ 0\end{pmatrix} - \begin{pmatrix}0\\ g\bar{h}^+_{i-1/2}\Delta b^+_{i-1/2}\\ 0\end{pmatrix} - \frac{\mathcal{C}_{i-1/2}}{2}\begin{pmatrix}\Delta b_{i-1/2}\\ 0\\ g\bar{b}_{i-1/2}\Delta b_{i-1/2}\end{pmatrix}.\end{aligned}$$

The above discretization exactly preserves the hydrostatic conditions by enforcing at a cell interface that $\Delta h = -\Delta b$, while the terms $g\bar{h}^-_{i+1/2}\Delta b^-_{i+1/2}$ and $g\bar{h}^+_{i-1/2}\Delta b^+_{i-1/2}$, which vanish for a first order scheme, enforce the hydrostatic condition by satisfying $\Delta h^\pm = -\Delta b^\pm$.

3.2. **Friction and drag terms treatment**

Concerning the treatment of the source term $\mathbf{S}_f$, at the second splitting step, we use (3.3) as a prediction without the friction and drag terms, i.e.

$$\mathbf{U}_i^\star = \mathbf{U}_i^n - \frac{\Delta t^n}{\Delta x}\left(\mathbf{F}_{i+1/2} - \mathbf{F}_{i-1/2} + \mathbf{S}_b^{i+1/2} + \mathbf{S}_b^{i-1/2}\right) \tag{3.3}$$

where for simplicity the forward Euler time stepping is presented with Δt^n being the current time step and $\mathbf{U}_i^n$ the average value at time t^n. At the second splitting step the following system of ODEs has to be solved

$$\frac{d\mathbf{U}}{dt} = \mathbf{S}_f(\mathbf{U}) \tag{3.4}$$

with initial condition $\mathbf{U}_i^\star$ calculated at the first step. Using the same strategy as in [25], the first two equations of the system can be explicitly solved in each cell I_i as

$$h_i^{n+1} = h_i^\star, \quad q_i^{n+1} = \frac{q_i^\star}{1 + \Delta t^n |q_i^\star| \dfrac{C_f}{(h_i^\star)^2}}. \tag{3.5}$$

The last equation for the energy, following from (2.3), is then

$$\frac{d\Psi_i}{dt} = -\frac{2C_r \Psi_i}{\Psi_i + \phi_s}\left(\frac{q_i}{h_i^2}\right)^3. \tag{3.6}$$

Integrating it, Ψ_i^{n+1} can be found in implicit form:

$$\Psi_i^{n+1} - \Psi_i^\star + \phi_s \ln\left(\frac{\Psi_i^{n+1}}{\Psi_i^\star}\right) = \frac{C_r}{C_f}\left(\frac{q_i^\star}{(h_i^\star)^2}\right)^2 \left(\frac{1}{\left(1 + \Delta t^n |q_i^\star| \dfrac{C_f}{(h_i^\star)^2}\right)^2} - 1\right) \tag{3.7}$$

which is then solved by the Newton-Raphson method.

3.3. **Higher-order spatial and temporal discretizations**

As it was mentioned in Section 3.1, a second-order spatial discretization can be obtained by properly define the left and right stated at a cell I_i interface. To this end, we utilize the classical MUSCL reconstruction technique, we refer for example in [26], which provides the following states at a cell interface for each of the components of $\mathbf{U}_i$ as.

$$u_{i+1/2}^L = u_i + 0.5 s(r_i)(u_i - u_{i-1}), \quad u_{i+1/2}^R = u_{i+1} - 0.5 s(r_{i+1})(u_{i+1} - u_i),$$

where

$$r_i = \frac{u_i - u_{i-1}}{u_{i+1} - u_i}$$

and $s(r_i)$ is a limiter function. In the present work the classical Van Leer slope limiter has been utilized in the numerical results presented later on in Section 4.

To achieve second-order accuracy in time the optimal, in the sense of the CFL condition, second-order two-stage Strong Stability Preserving (SSP) Runge-Kutta (RK) method has been implemented. This reads as follows

$$\mathbf{U}_i^{(1)} = \mathbf{U}_i^n + \Delta t^n \mathcal{L}(\mathbf{U}_i^n);$$
$$\mathbf{U}_i^{n+1} = \frac{1}{2}\mathbf{U}_i^n + \frac{1}{2}\mathbf{U}_i^{(1)} + \frac{1}{2}\Delta t^n \mathcal{L}(\mathbf{U}_i^{(1)})$$

where $\mathcal{L}(\mathbf{U})$ is the spatial operator from (3.3) and Δt^n denoted the time-step. It is noted that, the friction and drag term treatment is implemented at the end of each RK step. The stability of the numerical scheme is imposed by the usual CFL condition for explicit schemes and the time-step Δt^n is adaptively computed from it as

$$\Delta t^n = \text{CFL} \cdot \frac{\Delta x}{\max_i\{\mathcal{C}_{i+1/2}\}}$$

where $\mathcal{C}_{i+1/2}$ is computed as in Section 3.1 for each I_i computational cell. First-order schemes are stable if the CFL condition is respected for a CFL number less than one. However, one has to reduce by two (and sometimes by three) the time step to carry out simulations with the second-order scheme to preserve stability. Thus, the CFL value was set to 0.4 in all the computations performed in the next section, unless otherwise stated.

An general algorithmic view of the order that the variables are computed within the numerical scheme is given below.

Algorithm The splitting method for the SSWE
Step 1. Given the initial data at time level $n = 0$ for h, q and Ψ compute the total energy E.
Step 2. Compute the advective part (7) to obtain the prediction values $h_i^\star$, $q_i^\star$ and $E_i^\star$.
Step 3. Compute the prediction of the roller enstrophy $\Psi_i^\star$ from $E_i^\star$.
Step 4. Solve (9) and (11) to get h_i^{n+1}, q_i^{n+1} and Ψ_i^{n+1} to compute E_i^{n+1}.

Remark. We note here that, as it is well-known, using the Rusanov numerical flux in our finite volume approach it is expected to behave in a dissipative way thus, necessitating the use of relative fine meshes. However, this solver has good stability properties without needing to solve the Riemann problem and can be considered as a first approach in solving the extended SSWE. Furthermore, as shown in Section 3.1, it can be extended as to produce a well-balanced scheme. The development of more elaborate well-balanced finite volume schemes for the SSWE is not in the main scope of this presentation but it constitutes an interesting research problem which can benefit from further investigations.

4. Numerical tests and solutions

In this section, we present numerical tests and results to verify the ability of the proposed numerical scheme to approximate the SSWE model and the phenomena it aims to describe. More precisely, our main interested is for approximating non-stationary hydraulic jumps over constant and non-constant topographies which exhibit an oscillatory behavior in their toes and free surface. Further, and of equal importance, a family of exact solutions to the stationary SSWE is also derived.

4.1. Hydraulic jumps with different Froude numbers

These test cases were presented in [25] and are used here as to demonstrate the ability of the numerical scheme to reproduce the expected (non-stationary) behavior for non-stationary hydraulic jumps on a flat bottom. The hydraulic jump features depend on the upstream (of the jump) average Froude number (Fr_1). As it was demonstrated in [25], the jump toe (with position $x_1(t)$) oscillates for all Froude numbers greater than ~ 1.5. The main frequency of the oscillations decreases as Fr_1 increases while the oscillation amplitude increases.

In the cases presented here we consider a channel of length $L = 10$ m and given the values for ϕ_s, C_f and C_r, supercritical inflow conditions, at $x = 0$ m, are imposed by setting $h(0,t) = h_0$ m, $q(0,t) = q_0$

m^2/s and $\Psi(0,t) = 0$. At $x = L$ subcritical boundary conditions are obtained by imposing a blockage by a sharp-crested weir of height d_w with the flow given by the empirical relation [15]

$$q(L,t) = f(h) = \begin{cases} 0 & \text{if } h \leq d_w; \\ \frac{2}{3} C_d \sqrt{2g(h-d_w)^3} & \text{if } h > d_w, \end{cases} \tag{4.1}$$

where the discharge coefficient C_d is given by

$$C_d = \frac{\pi}{\pi + 2} + 0.08 \frac{h - d_w}{d_w}.$$

To compute the numerical flux $\mathbf{F}(\mathbf{U})_{N+1/2} = \mathbf{F}(\mathbf{U}_N^\star)$ at the outflow boundary cell N we need to estimate the $\mathbf{U}_N^\star$ values as a function of $\mathbf{U}_N$. From (4.1), the discharge value is set to

$$q_N^\star = f(h_N).$$

The second condition stems from the fact that Φ_N is the Riemann invariant transported by the flow at the boundary $x = L$ which give

$$\Psi_N^\star = \Psi_N.$$

Finally, the water depth $h_N^\star$ is computed by the outgoing characteristic as

$$u_N - u_N^\star + \int_{h_N^\star}^{h_N} \frac{\sqrt{gh + 3(\phi_s + \Psi_N)h^2}}{h} dh = 0.$$

The initial condition for h given in these test cases corresponds to the approximate description of the hydraulic jump by the SWE based on the famous Bélanger formula of sequential depths which results to

$$h(x,0) = \begin{cases} h_0 & \text{if } x \leq \frac{L}{10}; \\ \frac{1}{2} h_0 \left(-1 \sqrt{1 + 8Fr_0^2} \right) & \text{if } x > \frac{L}{10}, \end{cases} \tag{4.2}$$

where $Fr_0 = q_0 / \sqrt{g h_0^3}$ is the inflow Froude number. The rest of the initial conditions are $q(x,0) = q_0$ and $\Phi(x,0) = \phi_s$. In Figure 4.1 a schematic view of a hydraulic jump, of length L_r, forming in a wide rectangular channel is presented. The location of the jump is controlled by the downstream weir.

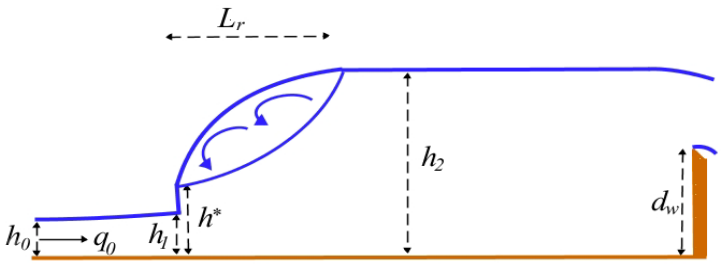

Figure 4.1. Schematic view of a hydraulic jump on a flat bed controlled by a downstream weir of height d_w

Following from [25], Table 4.1 gives the parameters values used for three test cases. Table 4.2 gives the target values for water depth h^* and large-scale enstrophy Ψ^*, upstream of the jump as derived by the Rankine-Hugoniot relations corresponding to the three balance equations for a stationary shock

in a horizontal channel, with h_2 being the depth at the end of the roller length L_r. The roller length can be estimated by the experimentally established empirical law [14]

$$L_r = h_1 160 \tanh\left(\frac{Fr_1}{20}\right) - 12h_1, \;\; 2.5 < Fr_1 < 16. \tag{4.3}$$

Case	**HJ2**	**HJ3**	**HJ4**
Average Fr_1	2.0	5.56	11.25
$q_0(m^2/s)$	0.0835	0.02286	0.0835
$h_0(m)$	0.05	0.011	0.016
C_f	0.00177	0.00236	0.00177
C_r	0.174	0.682	1.74
$\phi_s(s^{-2})$	0.87	4.09	2.76
$d_w(m)$	0.026	0.0344	0.135

Table 4.1. Test cases of non-stationary hydraulic jumps on a flat bed: parameter values used

Case	**HJ2**	**HJ3**	**HJ4**
$h_1(m)$	0.0562	0.012	0.0178
$h^\star(m)$	0.0966	0.0236	0.0354
$h_2(m)$	0.1313	0.0852	0.2556
$\Psi^\star$	23.23	1658.5	4295.5
$L_r(m)$ (from (4.3))	0.2218	0.3764	1.3884

Table 4.2. Test cases of non-stationary hydraulic jumps on a flat bed: target values

For the numerical results presented in this section, a relative fine grid is used of $N = 2000$ grid points as to capture the fine features of the oscillatory nature of the hydraulic jumps. Figure 4.2 presents the numerical results for case HJ2 for the water depth, h, and $\Phi = \Psi + \phi_s$. The numerical solution for water depth h is also compared with the stationary profile obtained, assuming $q = uh = cst$, by (numerically) solving the system of ODES

$$\frac{dh}{dx} = \frac{-C_f q^2 + 2C_r \Psi q^2/\Phi}{gh^3 + 3\Phi h^4 - q^2}; \tag{4.4}$$

$$\frac{d\Psi}{dx} = \frac{-2C_r \Psi q^2}{\Phi h^5}, \tag{4.5}$$

that depends only on the upstream given data while the numerical solution is that of the initial boundary value equations (2.1). System (4.4)-(4.5) can be derived from the steady-state momentum and energy equations of (3) for a horizontal channel ($b = 0$) since ϕ_s and $q = uh$ are constant. Figure 4.3 presents the oscillations of the jump toe position x_1 around its average value with a frequency of $\sim 1.1Hz$ and amplitude ~ 0.045 m. These results are in almost perfect agreement with those presented in [25].

Next, and in Figures 4.4 and 4.5 the results for test case HJ3 are presented. The comparison between the numerical solution and that of the stationary profile is presented for three times the roller length L_r after the jump. Again the jump toe oscillates around an average value with a frequency of $\sim 0.6Hz$ and amplitude ~ 0.098 m.

In Figures 4.6 and 4.7 the results for test case HJ4 are shown. The comparison between the numerical solution and that of the stationary profile is presented for almost two times the roller length L_r after the

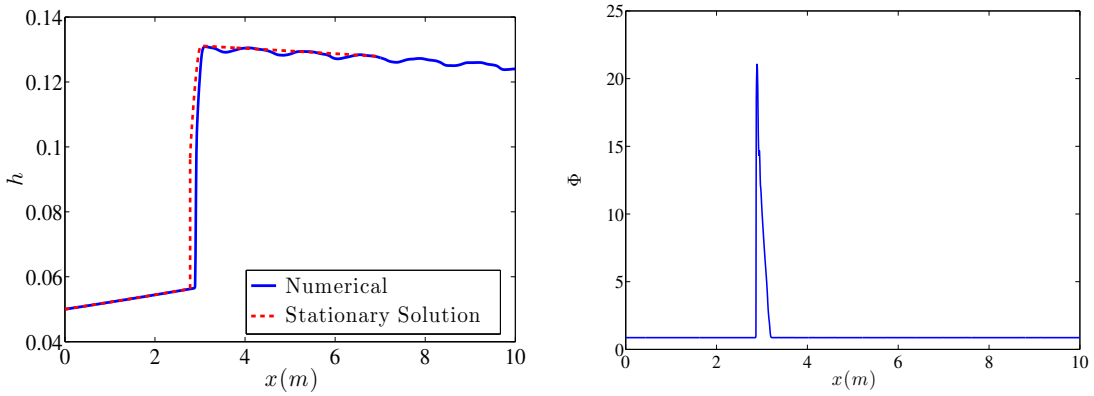

Figure 4.2. Numerical results at time $t = 650s$ for water depth h and total enstrophy Φ for test case HJ2

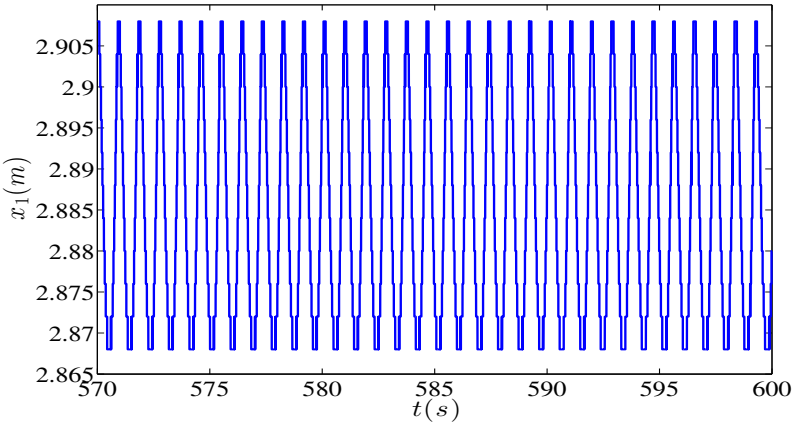

Figure 4.3. Oscillations in time of the jump toe position x_1 for test case HJ2

jump. The jump toe oscillates around an average value with a frequency of $\sim 0.227Hz$ and amplitude ~ 0.28 m.

Finally, in Table 4.3 the numerical values obtained for the target values in all three cases are presented along with the space width in which the toe position x_1 oscillates. For the roller length estimation, following [25], a good estimation for its end is considered to be when the large scale (roller) enstrophy $\Psi = \phi_s/2$. Comparing Tables 4.2 and 4.3 it can be seen that in all tests presented the expected oscillatory behavior of the hydraulic jump is demonstrated. The values of the water height obtained from the numerical simulation are very close to the ones predicted in Table 4.2 and only the values obtained for the enstrophy Φ are underestimated for cases HJ2 and HJ3. Nevertheless, the enstrophy exhibits the correct behavior with a large and sharp increase at the jump followed by a rapid decrease after the jump and up to the end of the roller. As such its maximum value is of relative importance to the obtained results, see for example [16], since all other values are in close agreement with the target ones. The oscillatory nature of the jump toe position in terms of frequency and amplitude is in almost perfect agreement with the results presented in [25] for all cases.

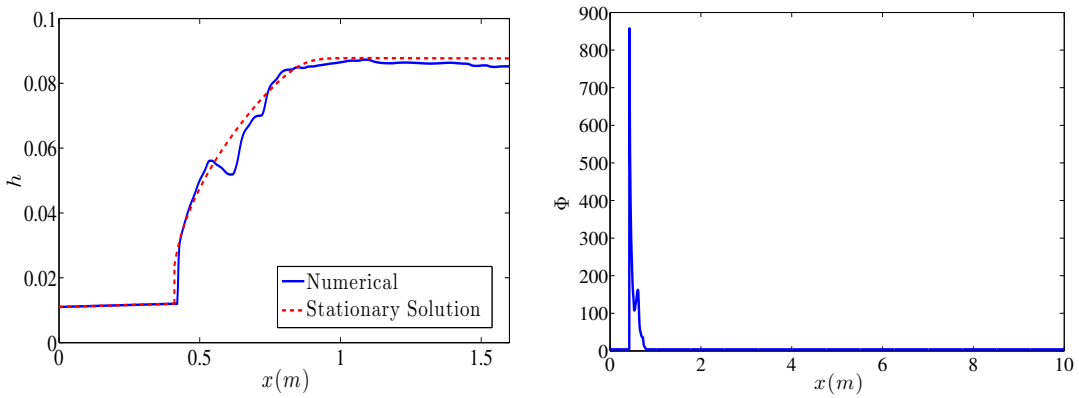

FIGURE 4.4. Numerical results at time $t = 550s$ for water depth h and total enstrophy Φ for test case HJ3

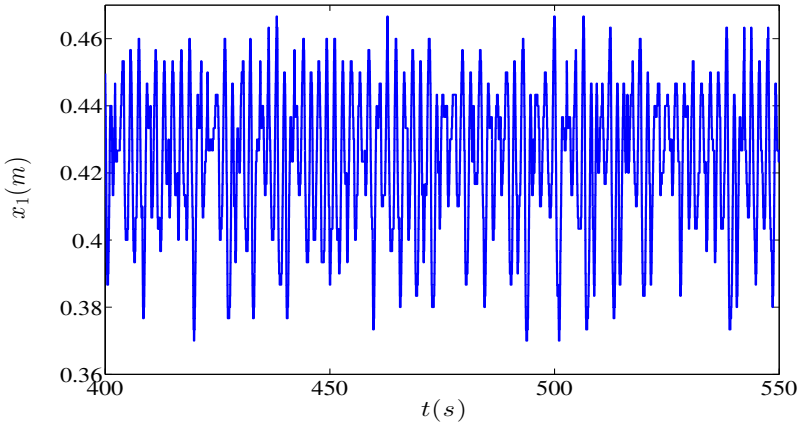

FIGURE 4.5. Oscillations in time of the jump toe position x_1 for test case HJ3

Case	**HJ2**	**HJ3**	**HJ4**
$h_1(m)$	0.0565	0.0118	0.0181
$h^\star(m)$	0.09862	0.0258	0.0363
$h_2(m)$	0.1308	0.0877	0.2588
$\Psi^\star$	21.4	855	3580
$L_r(m)$	0.215	0.38	1.46
$x_1(m)$	[2.868, 2.91]	[0.367, 0.465]	[0.85, 1.13]

TABLE 4.3. Test cases of non-stationary hydraulic jumps on a flat bed: numerical values

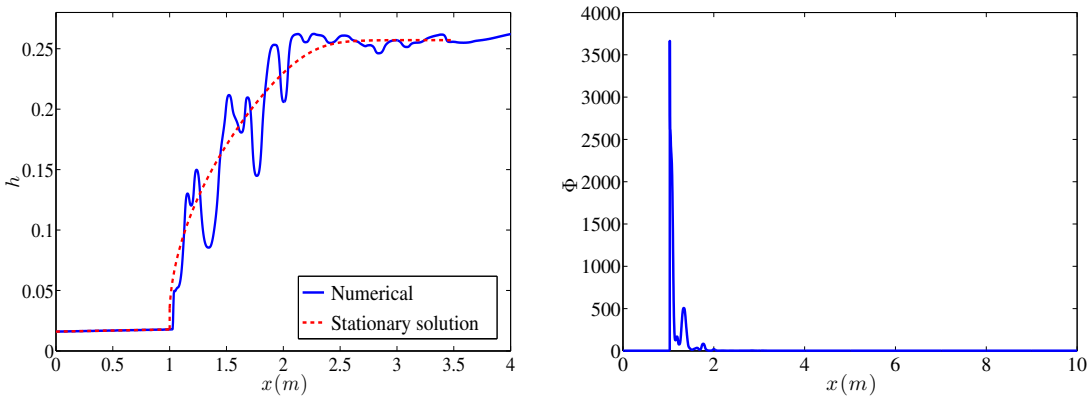

FIGURE 4.6. Numerical results at time $t = 350s$ for water depth h and total enstrophy Φ for test case HJ4

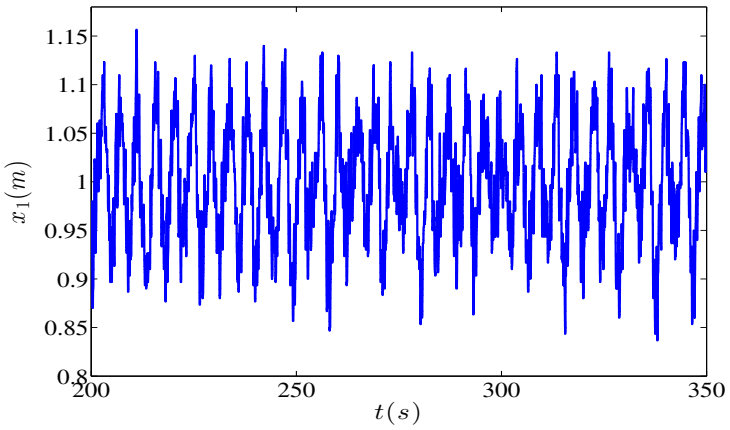

FIGURE 4.7. Oscillations in time of the jump toe position x_1 for test case HJ4

4.2. **Modified benchmark test problems of** [20]

Our aim here is to construct some analytic solutions to the steady SSWE over varying topography. Although these solutions are not for oscillatory hydraulic jumps (since their corresponding upstream Froude numbers are less than 1.7) their validity is of importance since they can serve as benchmark solutions to the model equations and numerical schemes. In [19, 20, 21], a set of realistic steady open channel flow test cases with analytic solution are given for the Saint-Venant equations. These test problems are often used for code benchmarking and comparison, we refer for example in [9, 10, 2, 27, 17, 18, 23, 7, 3] among others. Two such cases from [19, 20, 21] are utilized and modified here.

We first recall how these analytic solutions are constructed for the SWE by looking for steady piece-wise smooth solutions of the SWE characterized by a constant discharge q. Each smooth part of a solution is connected by a hydraulic jump. On each smooth part of the solution, the momentum equation becomes

$$[1 - Fr^2]h' + C_f Fr|Fr| = -b' \tag{4.6}$$

Let x_* be a point of discontinuity of the solution, the solution h_L on the left side of the discontinuity is arbitrary chosen and (4.6) is used to deduce the left bed slope b':

$$[1 - Fr^2(h_L)]h'_L + C_f Fr(h_L)|Fr(h_L)| = -b'_L. \tag{4.7}$$

By deriving relation (4.7), we can also compute the successive left derivatives of the bed in x_*: $b'_L(x_*), b''_L(x_*), \ldots, b_L^{(n)}(x_*)$. Then the Rankine-Hugoniot relation is used to deduce the water height h_R^* on the right side of the discontinuity. The form of the right solution $h_R(x)$ is then chosen as a function defined by n free parameters. These parameters are computed by solving the algebraic system requiring that $h_R^* = h_R(x_*^R)$ and that the bed at x_* and its $n-1$ successive derivatives are continuous. Using relation (4.6) and its derivatives, gives the $n-1$ equations $b'_R(x_*) = b'_L(x_*), b''_R(x_*) = b''_L(x_*), \ldots, b_R^{(n-1)}(x_*) = b_L^{(n-1)}(x_*)$ that together with $h_R^* = h_R(x_*^R)$ are solved for the n free parameters.

4.2.1. *Flow with a hydraulic jump on a varying bed*

The first example of analytic solutions constructed with this strategy is adapted from the Example 4 of [20]. This concerns a 1000 m long channel with a $q = 2$ m^2/s discharge. The flow is supercritical at inflow with a water depth of $h_0 = 0.543853$ m, it experiences an hydraulic jump at $x_* = 500$ m and then remains subcritical. The water depth is given by the expression:

$$h(x) = \begin{cases} 0.6673794620 - 0.1235887893\,\mathrm{e}^{-0.004\,x} & \text{for } 0 \le x < 500 \\ \\ 0.7415327355(1. + a_1\mathrm{e}^{-0.02\,x+10.0} + a_2\mathrm{e}^{-0.04\,x+20.0} & \text{for } 500 \le x \le 1000 \\ \quad +a_3\mathrm{e}^{-0.06\,x+30.0}) + 0.5932261883\,\mathrm{e}^{0.001\,x-1} & \end{cases} \tag{4.8}$$

and equation (4.6) allows to compute the corresponding bed slope. The values of the parameters in (4.8) are $a_1 = -0.2935698553, a_2 = 0.4080344466, a_3 = -0.4662074787$. Note that the values of the parameters a_1, a_2, a_3 are slightly different from the values given in [20]. This is due to the fact that the friction law used in [20] is the Manning one while here the Darcy-Weisbach law with a friction coefficient $C_f = 0.0053125$ has been used. We refer in Appendix A for an explanation and the relation between the two friction formulas.

While (4.8) is an exact solution of the nonlinear SWE it is not an exact solution of the shear shallow water model (2.1). Instead of (4.6), steady piece-wise smooth solutions of this model are characterized by the system of equations:

$$\text{momentum} \quad [1 - Fr^2(h) + 3\Phi h/g]h' + h^2\Phi'/g + C_f Fr(h)|Fr(h)| = -b' \tag{4.9.a}$$

$$\text{enstrophy} \quad h^5\Phi\Phi' = -2C_r|q|q(\Phi - \phi_s) \tag{4.9.b}$$

The same strategy as the one used in [20] can be employed to construct analytic solutions of (2.1) on a varying bed. However, this would result in a bed slope different from the one corresponding to the analytic solution of the shallow water equations. As our objective is also to compare the two models, we have found more interesting to use the same definition of the bed slope (that is thus computed as in [20] by (4.6)) and to numerically integrate the system of ordinary differential equation (4.9) to get the corresponding solution for the shear shallow water model (2.1). For this model the values of the small scale enstrophy ϕ_s and enstrophy dissipation coefficient C_r are constant and have been computed as recommended in [24, 25]:

$$\phi_s := 0.005 \cdot g/h_L(x_*),\ C_r := 0.0688 \cdot Fr(h_L(x_*))^{1.337}. \tag{4.10}$$

In this case the Froude number upstream of the jump is 1.21. Table 4.4 presents the values obtained by the analytic solutions of the SWE and the SSWE upstream and downstream of the jump as well as at the end of the channel for the water depth.

	h_L	h_R	Φ_L	Φ_R	$h(1000)$
SWE	0.6506535382	0.8405137415	–	–	1.3347490
SSWE	0.6506535382	0.8124613430	0.07538	0.156428	1.1856609

Table 4.4. Comparison of exact values between the shallow water model (SWE) and the shear shallow water model (SSWE) for the modified Example 4 of [20]

Figures 4.8 and 4.9 compare the exact results for water depth given by the two models on this bed slope as well as the numerical solution for the SSWE obtained with $N = 1000$ mesh points using a CFL value of 0.2. For the numerical solution of the SSWE the exact solution of the SWE for h is given as initial condition while the discharge was set to $q(x, 0) = 2m^2/s$. Setting the relative time variation for water depth as

$$R(h) = \sqrt{\sum_{i}^{N} \left(\frac{h_i^n - h_i^{n-1}}{h_i^n} \right)^2}$$

where h^n and h^{n-1} are the water depths at the current and previous time levels, the convergence criterion for a steady state was defined as $R(h) < 10^{-6}$. The convergence history is shown in Figure 4.9 (left panel) where the convergence criterion can be seen to be satisfied around 400s.

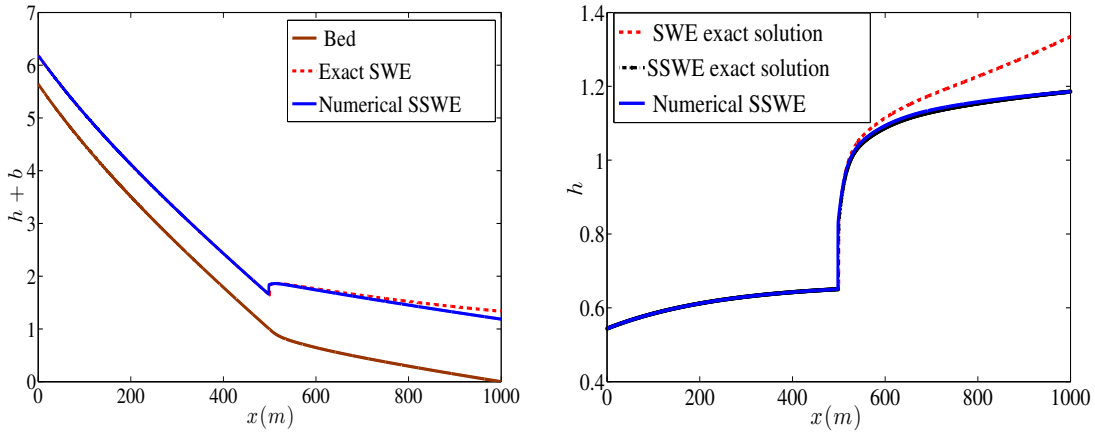

Figure 4.8. Water depth for the modified Example 4 case of [20]: Comparison between the shallow water model (SWE), the shear shallow water model (SSWE) and the numerical solution for SSWE

It can be seen that up to the hydraulic jump, the two analytic solutions cannot be distinguished. This is due to the fact that the solution for the enstrophy upwind to the discontinuity location x_* is given by : $\Phi \equiv \phi_s; \Phi' \equiv 0$ that is an exact solution of (4.9b). Then (4.9a) differs from the momentum equation of the shallow water model only by the term $3\phi_s h/g$ that is never larger than 10^{-6} for $x < x_*$ ($\phi_s = 0.07538574235$). On the discontinuity, the SSW model predicts an increase of the enstrophy and a smaller jump of the water height than in the SWE model. Downwind of the jump, the enstrophy

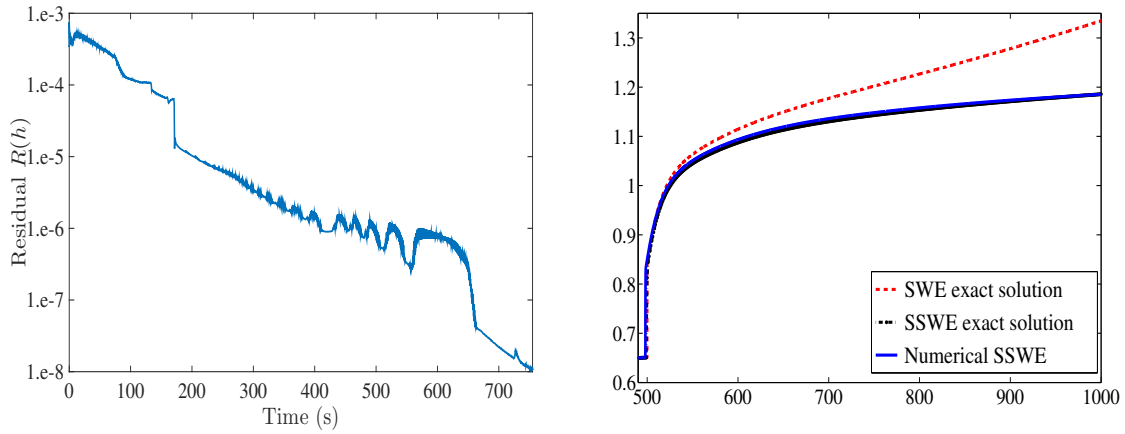

Figure 4.9. Residual convergence (left) and zoomed area of water depth for the modified Example 4 case of [20]: with comparison between the shallow water model (SWE), the shear shallow water model (SSWE) and the numerical solution for SSWE

relaxes very rapidly to the value of the small scale enstrophy. This is also confirmed numerically in Figure 4.10 (left panel), although the maximum value of Φ_R is slightly underestimated. Nevertheless, the numerical solution of the SSWE for the water depth is almost identical to the analytic solution. The water height slowly increases for the two models, with the value computed by the SSW model being continuously smaller than the value given by the SWE model. Further, the well-balance property of the numerical scheme is verified numerically on the right panel of Figure 4.10 where the computed discharge is presented. Only at the position of the jump a small glitch in the expected steady solution can be observed. This is a common behavior of all well-balanced schemes that satisfy the stagnant water well-balanced property. Convergence studies, verifying the order of accuracy of the numerical scheme using the exact solution from this test case are also given in Appendix B.

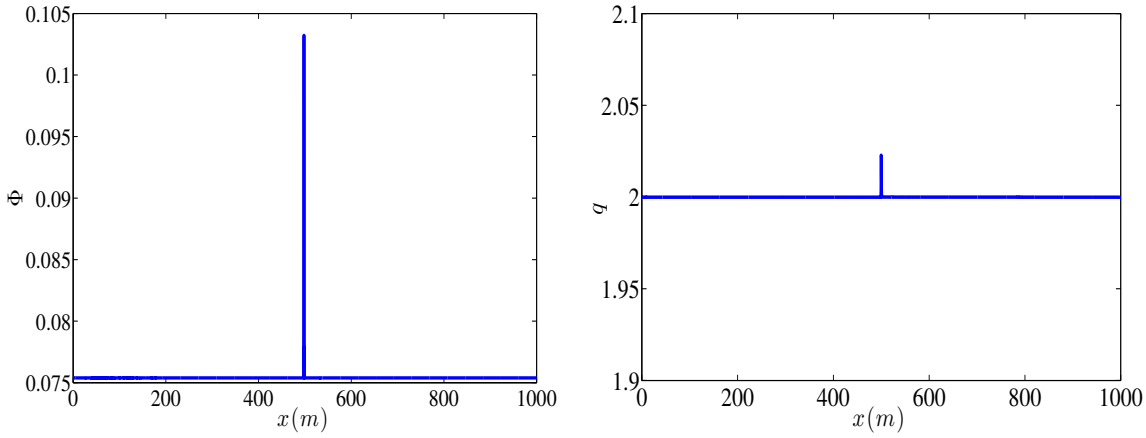

Figure 4.10. Numerical solution of the SSWE for total enstrophy (left) and discharge (right) for modified Example 4 of [20]

4.2.2. *Flow on constant slope followed by a hydraulic jump*

This test case is analogous to the one described in [19] (page 120) as problem 5. The domain is 100 m long and on the left of the discontinuity, located in $x_* = 50$ m, water flows with a constant depth of 0.7 m on a bed of constant slope. Then the bed flattens out smoothly and creates an hydraulic jump. This test case from [19] refers to a prismatic channel and uses the Manning friction law. In order to get results close to the ones in [19] we first have to estimate the discharge. For that we estimate, from the results in [19], the jump of the water height at the discontinuity from the Belanger relation

$$h_R/h_L = (\sqrt{1 + 8Fr_L^2} - 1)/2$$

which gives the jump in the water height as a function of the upwind Froude number. From that we deduce the Froude number on the left side of the discontinuity. With $h_R = 1.306421438$, this give a Froude number of 1.635459113 and a discharge of $q = 3$ m^2/s. It remains to compute the friction coefficient of the Darcy-Weisbach law. First, from the formula given in [19] (p. 117), we compute that the constant slope on the left is $b'_L = -0.06119282892$. Then using relation (4.7) with $h' \equiv 0$ we deduce the friction coefficient $C_f = 0.02287816294$. Then, the water depth is given by the expression:

$$h(x) = \begin{cases} 0.7 & \text{for } 0 \leq x < 50 \\ \\ \exp\left(-0.5(x - x_*)\right) \displaystyle\sum_{i=0}^{4} k_i \left(\frac{x - x_*}{100 - x_*}\right)^i + r(x) & \text{for } 50 \leq x \leq 100, \end{cases} \tag{4.11}$$

where $r(x) = 1.9 \exp(0.0005(x - 100))$. The k_0 coefficient has the value of $h_R(x_*) - r(x_*)$ in order for the water height on the right to be continuous while the other coefficients are given as: $k_1 = -9.314064506, k_2 = -73.51227688, k_3 = -225.0402141$ and $k_4 = 359.7904991$. The bed slope profile then results from expression (4.6). This suffices to define the test case for the SWE model. For the SSWE model we need in addition to define the values of the small scale enstrophy and dissipation coefficient of the enstrophy. Using again the relations given in [24, 25] we obtain:

$$\phi_s := 0.005 \cdot g/h_L(x_*) = 0.07007142855,\ C_r := 0.0688 \cdot Fr(h_L(x_*))^{1.337} = 0.1328081433. \tag{4.12}$$

Then, we numerically integrate the system of ordinary differential equations (4.9) to get the corresponding solution for the SSWE model.

Table 4.5 compare the exact results for the water depth given by the two models for this bed slope. Again the jump in water height obtained by the SSWE model is smaller than with the plain SWE. However, on the outflow water depth the difference is relatively small with the difference of water height between the two models being smaller than $6cm$. Figure 4.11 compares these exact solutions with the numerical solution obtained for the SSWE using $N = 1000$ grid points. As it can be seen, also in the area close to the jump, the numerical solution of the SSWE model is again in very close agreement with its analytic solution. Again, the enstrophy relaxes very rapidly to its pre-shock value, as shown also in Figure 4.12 (left panel) that displays its numerical solution along with the computed discharge.

	h_L	h_R	Φ_L	Φ_R	$h(100)$
SWE	0.7	1.306421438	–	–	1.900000001
SSWE	0.7	1.100077788	0.070071428	0.876972679	1.843596552

Table 4.5. Comparison of exact values between the shallow water model (SWE) and the shear shallow water model (SSWE) for the modified Problem 5 of [19]

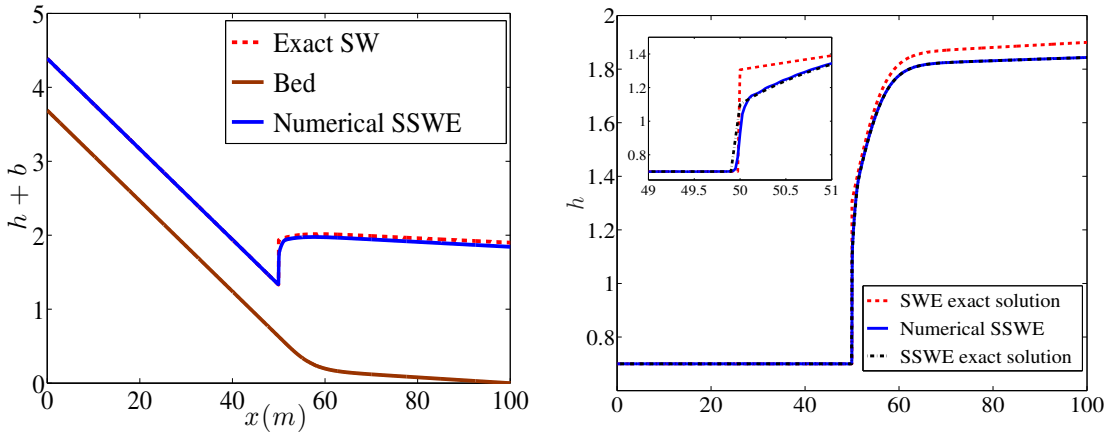

FIGURE 4.11. Water Depth for Example 5 case of [20]: Water depth for the modified Problem 5 of [19]: Comparison between the shallow water model (SWE), the shear shallow water model (SSWE) and the numerical solution the SSWE model

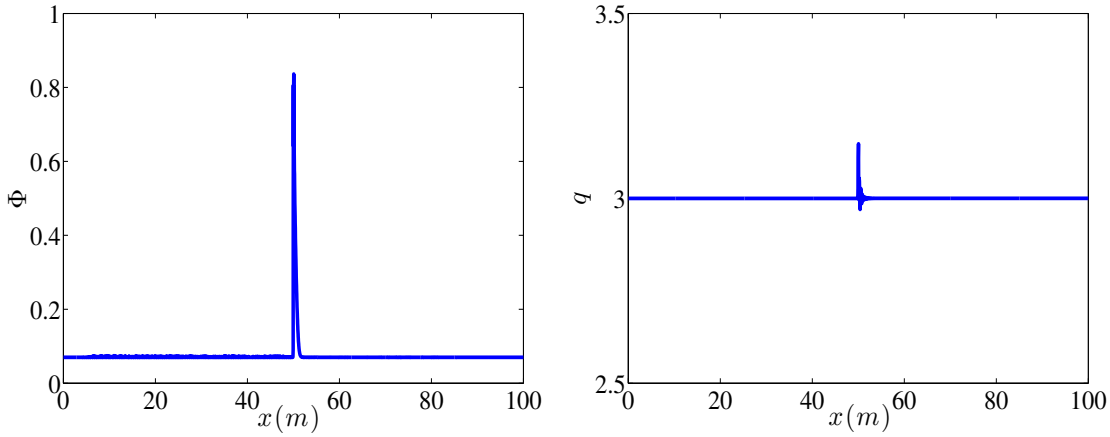

FIGURE 4.12. Numerical solution of the SSWE for total enstrophy (left) and discharge (right) for modified Problem 5 of [19]

4.3. **Flow over a parabolic bump-transcritical flow with a shock**

Here we present a modification of a classical test case, from [11], frequently used to asses the performance of well-balanced shock-capturing numerical schemes for approximating steady-state solution for the SWE with topography. If bottom friction is not considered, an analytic solution is available for testing the water level calculations for the SWE. Here, we aim to present the numerical solution obtained by solving the SSWE with all source terms present and asses its behavior. In his test case, the domain length is $L = 25$ m with a topography given by:

$$b(x) = \begin{cases} 0.2 - 0.05(x-10)^2 & \text{if } 8\text{m} < x < 12\text{m}, \\ 0 & \text{else.} \end{cases}$$

We choose for initial conditions

$$h(x,0)+b(x)=0.33\text{ m}\quad\text{and}\quad q(x,0)=0\text{ m}^2/\text{s}$$

and the following boundary conditions

$$\begin{cases}\text{upstream}: q=0.18m^2/s,\\ \text{downstream}: h=0.33m\end{cases}.$$

Due to the steep change in bed elevation, the flow changes from subcritical to supercritical and back to subcritical.

The $C_f=f/8=0.001616907601743$ friction coefficient in this case was estimate following [25] by the formula [15]

$$\frac{1}{\sqrt{f}}=2\log_{10}\left(Re\sqrt{f}\right)-0.8$$

where $Re=4q/\nu$ is the Reynolds number with $\nu=1.309\cdot10^{-6}$ being the kinematic viscosity. For the SSWE equations the values for $\phi_s=0.005\cdot g/h_1=0.607129595246937$ and the $C_r=0.0688F_1^{1.337}=0.235228180190780$. Since the values h_1 and F_1 at the jump toe were not known for the SSWE, these were based on estimates from the numerical results obtained for the SWE solution with friction. The upstream of the jump average Froude number, Fr_1, used to obtain the above values was 2.4 thus, it is expected that the jump toe will oscillate near some average value.

In Figure 4.13 a comparison is presented between the exact SWE solution (with no friction present) and that obtained for the SSWE at $t=200$ s using a relatively fine mesh of $N=1000$ grid points. For the SSWE the intensity of the jump is lower compared to that of the SWE. The computed total enstrophy, presented in Figure 4.14 (left panel), exhibits the expected behavior i.e. downwind of the jump the enstrophy relaxes very rapidly to the value of the small scale enstrophy. In Figure 4.14 (left panel) the computed discharge is given. More importantly, Figure 4.15 presents the oscillations of the jump toe position x_1 around its average value with an amplitude of ~ 0.05 m. Finally, the "theoretical" value of the roller length $L_r=1.1035$, obtained from (4.3), closely approximated by the numerical results which gives a value of 1.180.

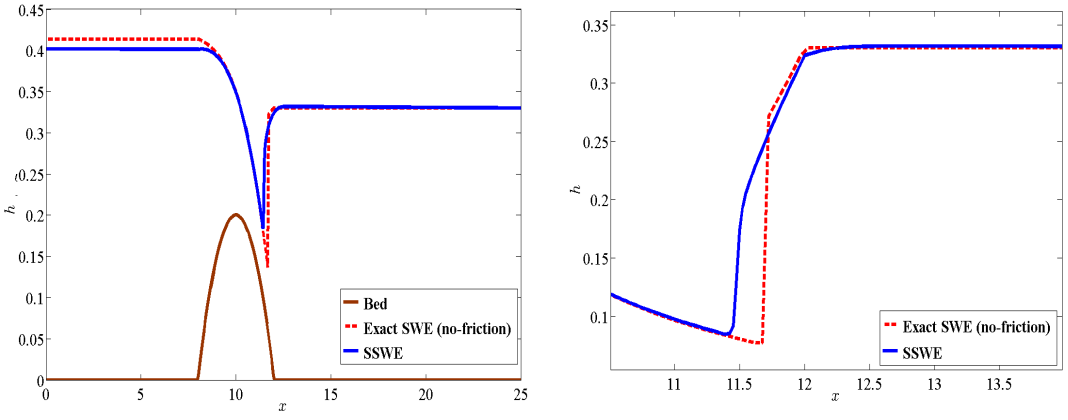

Figure 4.13. Water level and topography for the SWE and SSWE (left) and zoom at the water depth around the hydraulic jump area for the transcritical flow over a parabolic bump

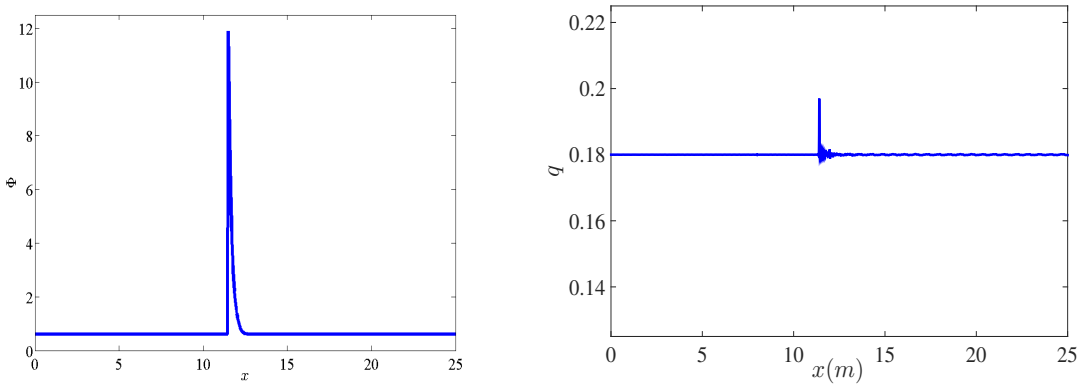

FIGURE 4.14. Numerical total enstrophy(left) and discharge (right) for the transcritical flow with a hydraulic jump over a parabolic bump

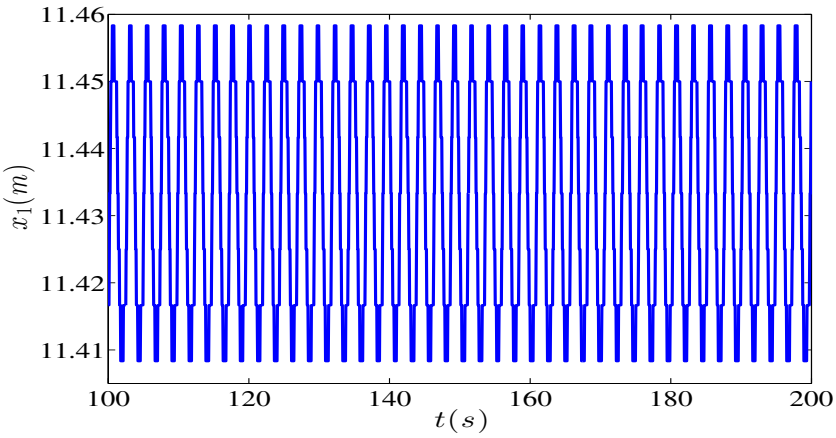

FIGURE 4.15. Position of the jump toe $x_1(t)$ for the transcritical flow with a hydraulic jump over a parabolic bump

4.4. **Experimental forced hydraulic jump**

Recently, in [6], an experimental and numerical investigation was presented for the developing stages of forced hydraulic jumps in inclined beds. The main objective of this study was to assess the free surface and velocity field from a forced hydraulic jump by using nonintrusive measuring techniques and a mesh-free numerical method. The test case considered here is for an inclination angle of 5^o in a channel of $L = 1.14$ m long.

A weir of height $d_w = 0.03$ m was placed at the downstream end of the channel. The inflow conditions consist of a discharge $q_0 = 5.608 \cdot 10^{-3}$ m^2/s and $h_0 = 0.01$ m. The rest of the parameters used for the SSWE have been computed according to the formulas given in Section 4.3. Based on measured average values of $Fr_1 = 3.96$ and $h_1 = 0.005858$ at the toe of the hydraulic jump in the experimental data, this gives $C_r = 0.433218407749443$, $C_f = 0.003369082820920$ and $\phi_s = 8.373175770887171$. Initially,

the slope is considered dry and numerically an artificially bed wetting with a wetting parameter of 10^{-6} was implemented [26].

In the experiments, the development of the forced hydraulic jump started after the fluid contacted the weir and a surge started to develop towards the upstream direction. This backward propagation is essential to the formation of such jumps. This backward propagation eventually stopped in time and it was observed that the toe of the jump continuously oscillated but the entire structure of the jump became gradually approximately consistent. In the experiment the jump is formed around $t = 4$ s. Although it cannot be excluded that in the initial stages, the flows exhibits some 3D phenomena, the agreement between the experimental results and the 2D numerical simulations reported in [6] shows that this experiment can serve as a concrete test for the 1D model considered here to test its ability to reproduce some important features of forced hydraulic jumps.

Fig. 4.16 presents the comparison between experimental measurements and the numerical solution obtained with the SSWE and the SWE at $t \approx 4$ s for the water depth using $N = 500$ mesh points and a CFL value of 0.25. In Fig. 4.16 approximately the last 30 cm of the channel are shown, since

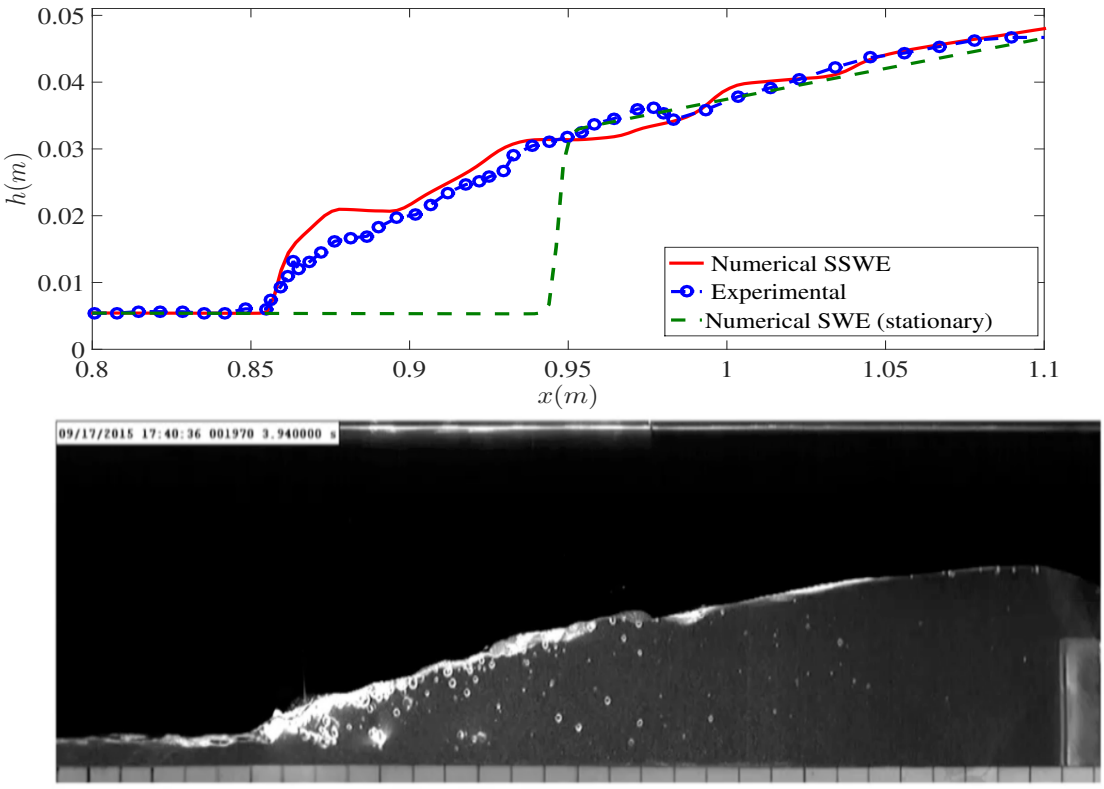

Figure 4.16. Water depth for the forced hydraulic jump experiment: comparison between numerical solution and experimental data (top) and experimental snapshot (bottom) at $t \approx 4s$

that was the area where experimental measurements where recorded, along with a snapshot, obtained with a high-speed camera. As expected, the SWE produce a stationary solution while the SSWE follows relatively close the experimental data at this time which corresponds to the initial stage of formation of the hydraulic jump. Although at the initial stages the numerical model is late in describing

the phenomena, also due to the artificial wetting used, the simulated jump gradually matched the experimental data. Figure 4.17 presents the total enstrophy and velocity profiles as computed by the numerical scheme. The predicted roller length was $L_r \approx 0.135$ m. Figure 4.18 presents the comparison for the free surface between the numerical and experimental data at later time instances. The shift of the jump toe is evident and the numerical solution gives a relatively accurate representation of the free surface variation. Finally, the oscillatory nature of the computed hydraulic jump is evident from the recording of the toe position x_1 around an average value as presented in Figure 4.19.

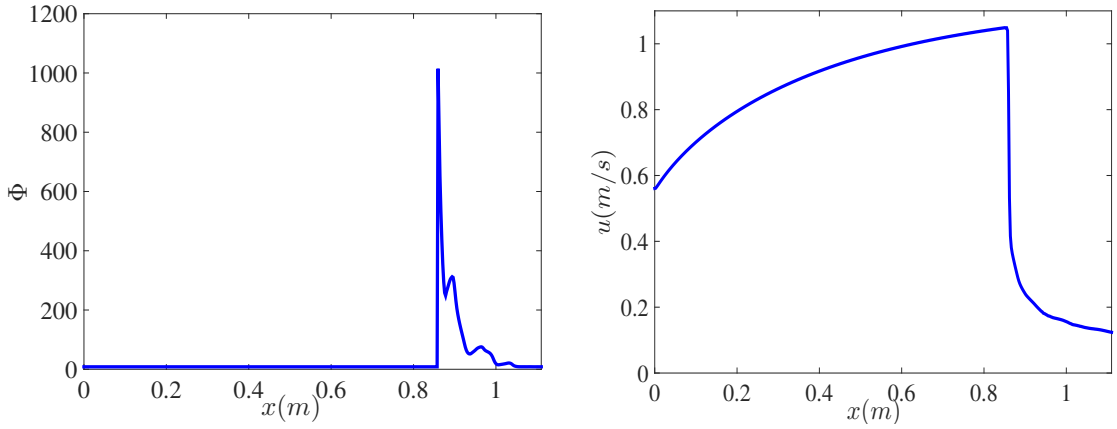

Figure 4.17. Total enstrophy (left) and velocity (right) for the forced hydraulic jump experiment

5. Conclusions

An extension and numerical solution of a previously developed two-parameter mathematical model describing shear shallow water flows was presented to study its potential of simulating turbulent hydraulic jumps. The mathematical model called the shear shallow water equations (SSWE) consists a conservative hyperbolic system with source terms present with two adjustable parameters, that have a well-defined physical interpretation, the wall enstrophy and energy dissipation coefficient. The SSWE were extended here in a straightforward manner as to incorporate arbitrary non-constant topographies without any adjustments to the model's parameters. To this end, a conservative second-order, in space and time, finite volume scheme was developed to numerically approximate the extended model. The proposed scheme satisfies the well-balance property for quiescent flows over topography. Several numerical test where performed as to access the ability of the numerical model to predict the formation of turbulent hydraulic jumps for upstream (to the jumps) Froude numbers larger than 1.7. The model was capable of predicting the oscillatory nature of such jumps, a phenomenon well-documented in the literature, and several characteristic such as the free surface evolution and jump roller length satisfactorily. Comparisons with experimental data of a forced hydraulic jump were also presented with satisfactory results, given the 1D nature of the model. Finally, an important contribution of this work is the derivation of a set of new analytic steady-state solutions to the SSWE model over variable topography. These exact solutions, although not for oscillatory hydraulic jumps, can serve as benchmark solutions for the validation of any numerical scheme aiming to approximate the model equations.

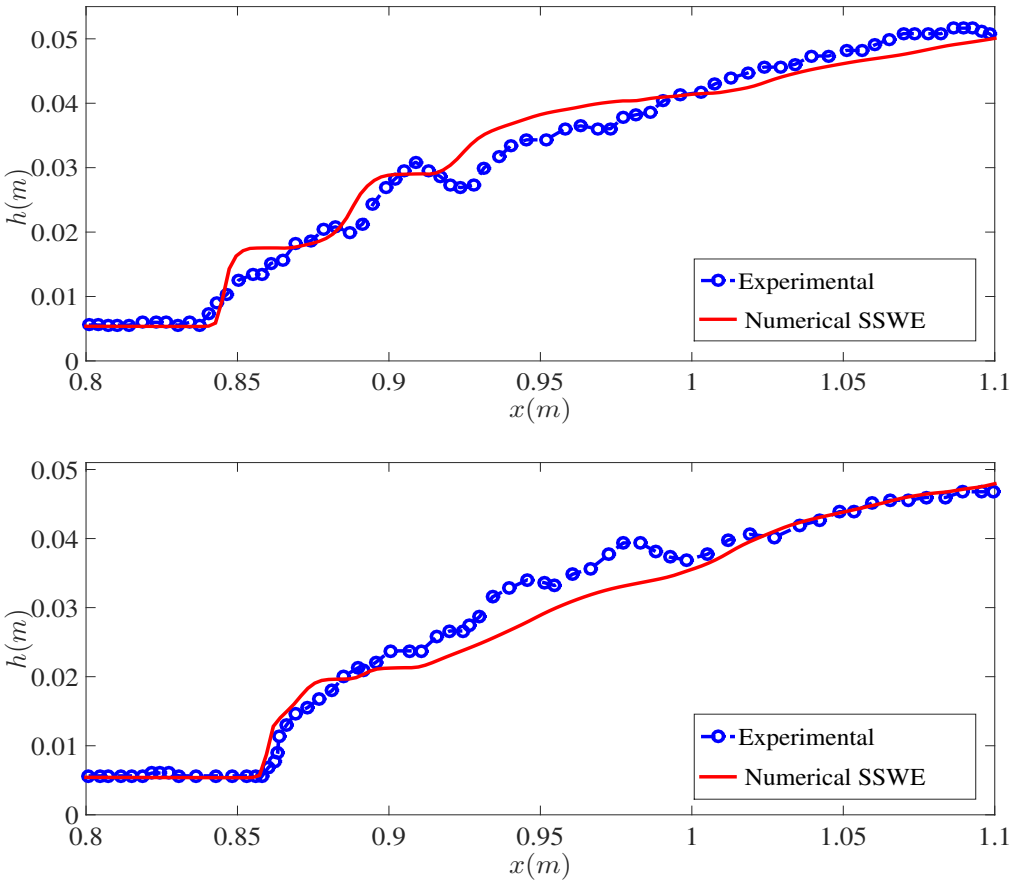

Figure 4.18. Water depth for the forced hydraulic jump experiment: comparison between numerical solution and experimental data at $t \approx 5.5$ s (top) and $t \approx 7$ s (bottom)

Acknowledgment

This work originates from visits of Yih-Chin Tai to Inria Sophia-Antipolis and of H. Guillard to the National Center for Theoretical Sciences (NCTS) of National Tawain University in the framework of the Inria-MOST Associate team program AMoSS. H. Guillard acknowledges the warm hospitality of NCTS and of the Technical University of Crete during the completion of this work. A.I. Delis wishes to thank the INRIA-Nice Sophia Antipolis University team CASTOR for its hospitality while contracting part of the presented research. The authors would also like to thank Boniface Nkonga, Mario Ricchiuto and Sergey Gavrilyuk for fruitful discussions on the SSWE model and its numerical approximation.

Appendix A. Friction formulae relation

We first recall that the Saint-Venant (SV) system results from an integration of the SWE along the cross-section of the channel. In [19, 20, 21] the analytic solutions are derived for the Saint-Venant (SV) equations for *prismatic channels* using the Manning friction formula. Instead of this friction formula, the present work uses the Darcy-Weisbach (DW) formula. Hence, a connection between the SV equations and SWE also in terms of the Darcy-Weisbach (DW) is given here. Considering a

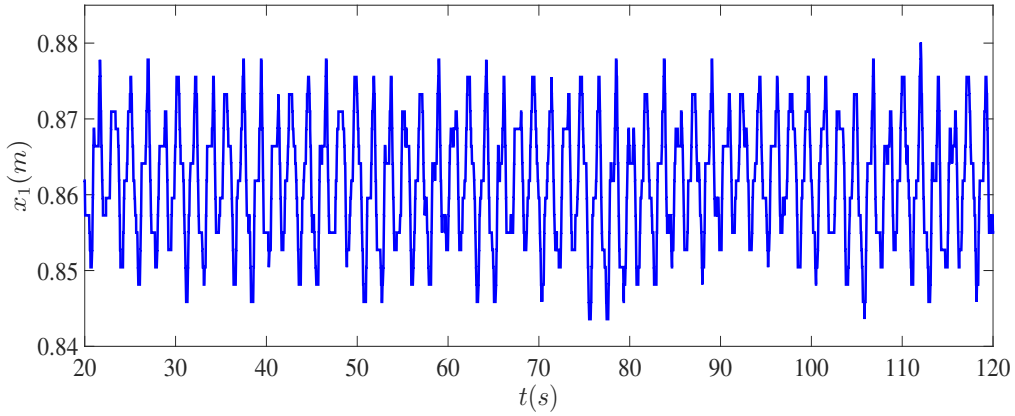

Figure 4.19. Oscillations in time of the jump toe position x_1 for the experimental forced hydraulic jump test case

prismatic rectangular channels with constant width B, wetted cross-sectional area $A = Bh$, wetted perimeter $P = B + 2h$ and constant discharge $Q = Au = Bhu = Bq$ the resulting SWE with topography and friction are given as [12]

$$\frac{\partial h}{\partial t} + \frac{\partial q}{\partial x} = 0 \tag{A.1}$$

$$\frac{\partial q}{\partial t} + \frac{\partial}{\partial x}\left(q^2/h + gh^2/2\right) = -gh(\partial_x b - S_f^M) \tag{A.2}$$

where the friction slope in terms of the Manning coefficient is given as

$$S_f^M = \frac{Q|Q|n_m^2 P^{4/3}}{A^{10/3}} = \frac{Q|Q|n_m^2\,(B+2h)^{4/3}}{Bh^{10/3}} = \frac{q|q|n_m^2\left(1+\frac{2h}{B}\right)^{4/3}}{h^{10/3}} \tag{A.3}$$

that is, if it is to represent the friction term coming from SV to SWE it should be with a modified friction constant

$$\widetilde{n}_m^2 = n_m^2\left(1+\frac{2h}{B}\right)^{4/3}. \tag{A.4}$$

This may be expanded assuming $B \gg h$ as

$$\widetilde{n}_m^2 = n_m^2\left(1+\frac{4}{3}\frac{2h}{B}+\frac{2}{9}\left(\frac{2h}{B}\right)^2+\cdots\right).$$

To get a global (in all the channel) estimate for $\widetilde{n}_m$ from n_m the critical depth can used i.e. from $Fr = u/\sqrt{gh} = 1$ resulting in

$$h_{cr} = \left(\frac{q^2}{g}\right)^{1/3}.$$

Thus, for the SWE the Manning friction slope maybe written as

$$S_f^M = \frac{q|q|\widetilde{n}_m^2}{h^{10/3}} = \frac{u|u|\widetilde{n}_m^2}{h^{4/3}} \tag{A.5}$$

Since in the SSWE the DW formula is used i.e.

$$S_f^{DW} = f\frac{q|q|}{8gh^3} = f\frac{u|u|}{8gh}, \tag{A.6}$$

we can approximate f from Manning's formula above as

$$f \approx \frac{8g\widetilde{n}_m^2}{h^{1/3}}. \tag{A.7}$$

In the SSWE derivation we use in the momentum equation

$$-ghS_f^{DW} = -f\frac{u|u|}{8} = -C_f|u|u$$

which results in the obtained form of $\mathbf{S}_f$ in (2.1).

The analytical solutions for the SWE derived in Section 4 for $h(x)$ and slope b' satisfy then the following relation for each friction term used

$$b' = \left(1 - \frac{q^2}{gh^3}\right)h'(x) + \frac{fq^2}{8gh^3} \quad \text{(DW formula)}.$$

which corresponds to (4.6).

Appendix B. Mesh convergence study

For the new exact solution from Section 4.2.1 a convergence analysis is performed by first only simulating the smooth part of the solution downstream of the hydraulic jump i.e. for $x \in (500, 1000]$ where the flow regime is smooth and purely subcritical (see Figure 9). For the convergence studies we define the L^1 and L^∞ errors for water depth as

$$L^1(h) = \Delta x \sum_1^N |h_i^n - h_i^{ex}| \quad \text{and} \quad L^\infty(h) = \max_{i=1,\dots,N} |h_i^n - h_i^{ex}|$$

were $(h_i^{ex})_{i=1,\dots,N}$ and $(h_i^n)_{i=1,\dots,N}$ are, respectively, the exact and the approximate cell mean values at a final time $t^n = t_f$. Computations were carried out, for different meshes, until the final time $t_f = 500s$ with the first- and second-order versions of the numerical scheme with a CFL=0.1. The reduced CFL value used is justified by the need to ensure that the errors incurred by the temporal integration are negligible. At this time the L^1 and L^∞ errors were several orders of magnitude higher that the corresponding relative variations of the flow variables between consecutive time steps, meaning that, in practice, a steady-state regime has been reached.

The errors for the different meshes and convergence rates are given in Table B.1. The errors computed point out that the second-order convergence is close to optimal for both norms, while the corresponding errors for the first-order version of the scheme are much higher. It is noted that, a similar behavior is obtained for the other flow variables as well.

	First-order scheme				Second-order scheme			
Δx	$L^1(h)$	Order	$L^\infty(h)$	Order	$L^1(h)$	Order	$L^\infty(h)$	Order
5	4.162		6.28e-2		1.836		3.89e-2	
2.5	2.010	1.05	2.98e-2	1.07	6.49e-1	1.50	1.29e-2	1.59
1.25	1.028	0.96	1.54e-2	0.95	2.12e-1	1.61	4.13e-3	1.64
0.625	5.23e-1	0.97	7.89e-3	0.96	5.75e-2	1.88	1.17e-3	1.82
0.3125	2.65e-1	0.98	4.03e-3	0.97	1.53e-2	1.91	3.19e-4	1.87
0.15625	1.34e-1	0.98	2.05e-3	0.97	4.04e-3	1.92	8.52e-5	1.90

Table B.1. Water depth (h) L^1 and L^∞ errors and convergence rates for the first- and second-order schemes for the half domain solution

Next, in Table B.2, we present convergence results for the full domain solution in terms of the L^1 norm for water depth and water discharge $q = hu$. As expected, due to the presence of the hydraulic jump the order of the second-order scheme drops to one but the accuracy of the results is much greater compared to that of the first-order scheme.

	First-order scheme				Second-order scheme			
Δx	$L^1(h)$	Order	$L^1(q)$	Order	$L^1(h)$	Order	$L^1(q)$	Order
5	30.325		100.06		3.251		1.537	
2.5	15.529	0.96	54.630	0.87	1.485	1.13	4.96e-1	1.66
1.25	7.919	0.97	27.740	0.97	7.51e-1	0.98	1.78e-1	1.45
0.625	4.118	0.95	13.975	0.99	3.79e-1	0.98	7.50e-1	1.24
0.3125	2.148	0.95	7.007	0.99	1.92e-1	0.98	3.43e-1	1.13
0.15625	1.112	0.95	3.550	0.98	9.78e-2	0.97	1.68e-1	1.03

Table B.2. Water depth (h) and discharge (q) L^1 errors and convergence rates for the first- and second-order schemes for the full domain solution

References

[1] A. Bermudez and M. E. Vázquez. Upwind methods for hyperbolic conservation laws with source terms. *Computers & Fluids*, 23(8):1049–1071, 1994.

[2] J. Burguete and P. García-Navarro. Efficient construction of high-resolution TVD conservative schemes for equations with source terms: Application to shallow water flows. *International Journal for Numerical Methods in Fluids*, 37(2):209–248, 2001.

[3] D. Caviedes-Voullième and G. Kesserwani. Benchmarking a multiresolution Discontinuous Galerkin shallow water model: Implications for computational hydraulics. *Advances in Water Resources*, 86:14–31, 2015.

[4] Y. Chachereau and H. Chanson. Free-surface fluctuations and turbulence in hydraulic jumps. *Experimental Thermal and Fluid Science*, 35:896–909, 2011.

[5] H. Chanson. Convective transport of air bubbles in strong hydraulic jumps. *Int. J. Multiphase Flow*, 36:798–814, 2010.

[6] C.-K. Cheng, Y.-C. Tai, and Y.-C. Jin. Particle image velocity measurement and mesh-free method modeling study of forced hydraulic jumps. *Journal of Hydraulic Engineering*, 143(9):04017028, 2017.

[7] O. Delestre, C. Lucas, P.-A. Ksinant, F. Darboux, C. Laguerre, T.-N.-T. Vo, F. James, and S. Cordier. SWASHES: A compilation of shallow water analytic solutions for hydraulic and environmental studies. *International Journal for Numerical Methods in Fluids*, 72:269–300, 2013.

[8] A. I. Delis, M. Kazolea, and N. A. Kampanis. A robust high-resolution finite volume scheme for the simulation of long waves over complex domains. *International Journal for Numerical Methods in Fluids*, 56(4):419–452, 2008.

[9] A. I. Delis and C. P. Skeels. TVD schemes for open channel flow. *International Journal for Numerical Methods in Fluids*, 26(7):791–809, 1998.

[10] A. I. Delis, C. P. Skeels, and S. C. Ryrie. Implicit high-resolution methods for modelling one-dimensional open channel flow. *Journal of Hydraulic Research*, 38(5):369–381, 2000.

[11] N. Goutal and F. Maurel. Proceedings of the 2nd workshop on dam-break wave simulation. Technical Report HE-43/97/016/B, Départment Laboratoire National d'Hydraulic, Groupe Hydraulic Fluviale Electricité de Fracne, France, 1997.

[12] W. H. Graf and M. S. Altinakar. *Fluvial hydraulics: flow and transport processes in channels of simple geometry*. Wiley, 1998.

[13] W. H. Hager and R. Bremen. Classical hydraulic jump: sequent depths. *J. Hydraul. Res.*, 27:565–585, 1989.

[14] W. H. Hager, R. Bremen, and N. Kawagoshi. Classical hydraulic jump: lenght of roller. *J. Hydraul. Res.*, 28:591–608, 1990.

[15] F. M. Henderson. *Open Channel Flow*. MacMillan, 1966.

[16] K. A. Ivanova, S. L. Gavrilyuk, B. Nkonga, and G. L. Richard. Formation and coarsening of roll-waves in shear shallow water flows down an inclined rectangular channel. *Computers & Fluids*, 159:189–203, 2017.

[17] G. Kesserwani, R. Ghostine, J. Vazquez, A. Ghenaim, and R. Mosé. Application of a second-order Runge-Kutta discontinuous Galerkin scheme for the shallow water equations with source terms. *International Journal for Numerical Methods in Fluids*, 56(7):805–821, 2008.

[18] S.-H. Lee and N. G. Wright. Simple and efficient solution of the shallow water equations with source terms. *International Journal for Numerical Methods in Fluids*, 63(3):313–340, 2010.

[19] I. MacDonald. *Analysis and computation of steady open channel flows*. PhD thesis, University of Reading, 1996.

[20] I. MacDonald, M. J. Baines, N. K. Nichols, and P. G. Samuels. Steady open channel test problems with analytic solutions. Technical Report 3/95, University of Reading, 1995.

[21] I. MacDonald, M. J. Baines, N. K. Nichols, and P. G. Samuels. Analytic benchmark solutions for open-channel flows. *Journal of Hydraulic Engineering*, 123(11):1041–1044, 1997.

[22] K. M. Mok. Relation of surface roller eddy formation and surface fluctuation in hydraulic jumps. *Journal of Hydraulic Research*, 42(2):207–212, 2004.

[23] M. Morales-Hernandez, P. García-Navarro, and J. Murillo. A large time step 1d upwind explicit scheme (CFL>1): Application to shallow water equations. *Journal of Computational Physics*, 231(19):6532–6557, 2012.

[24] G. L. Richard and S. L. Gavrilyuk. A new model of roll waves: comparison with brock's experiments. *Journal of Fluid Mechanics*, 698:374–405, 004 2012.

[25] G. L. Richard and S. L. Gavrilyuk. The classical hydraulic jump in a model of shear shallow-water flows. *Journal of Fluid Mechanics*, 725:492–521, 005 2013.

[26] E. F. Toro. *Shock-Capturing Methods for Free-Surface Shallow Flows*. John Wiley and Sons, Ltd, 1998.

[27] M.-H. Tseng. Improved treatment of source terms in TVD scheme for shallow water equations. *Advances in Water Resources*, 27(6):617–629, 2004.

[28] M. E. Vázquez-Cendón. Improved treatment of source terms in upwind schemes for the shallow water equations in channels with irregular geometry. *Journal of Computational Physics*, 148(2):497–526, 1999.